Synthesis of FAU(Y)- and MFI(ZSM5)-nanosized crystallites for catalytic cracking of 1,3,5-triisopropylbenzene

P. Morales-Pacheco [a,∗], J.M. Domínguez [b], L. Bucio [a], F. Alvarez [b], U. Sedran [c], M. Falco [c]

[a] Instituto de Física, UNAM, Apdo. Postal 20-374, 01000 México, D.F., Mexico
[b] Instituto Mexicano del Petróleo, Programa de Ingeniería Molecular, Eje Central L. Cárdenas No. 152, 07730, México, D.F., Mexico
[c] Instituto de Investigaciones en Catálisis y Petroquímica, INCAPE (FIQ, UNL-CONICET), Santiago del Estero 2654, (3000) Santa Fe, Argentina

ABSTRACT

Nanocrystals of FAU(Y) and MFI(ZSM5) zeolites were synthesized from clear solutions at 80–95 °C under autogen and atmospheric pressures, respectively. The X-ray diffraction (XRD) patterns confirm the structural features reported for FAU(Y) and MFI(ZSM5). Similarly, Fourier transform infrared spectroscopy (FTIR) with KBr shows the bands arising from typical structural groups of FAU(Y) and MFI(ZSM5), i.e., $455–462 \, cm^{-1}$ and $555–560 \, cm^{-1}$. The mean crystallites size was measured by transmission electron microscopy (TEM) and it was determined also by Rietveld's method using Scherrer's equation; with similar results between 20 and 40 nm. Also, a cubic morphology for FAU(Y) crystallites and a disk-like habit for MFI(ZSM5) were verified together with the typical dimensions of the pore system and symmetry, i.e., pore diameters were between 0.74 and 0.56 nm for FAU(Y) and MFI(ZSM5). Theoretical images were calculated using HRTEM (Cerius^2) program and these were compared with the experimental ones, thus matching the corresponding typical structural parameters. The textural properties were determined by N_2 adsorption–desorption (BET) and typical surface areas of 658 and 495 m^2/g were obtained for the nanosized materials. After ion-exchanging NH_4NO_3 ammonia was removed by calcination (i.e., 550 °C) and the total acidity was measured, i.e. 1190 and 1084 $\mu mol(Py)/g$ (cat) at 25 °C and 84 and 34 $\mu mol(Py)/g$ (cat) at 400 °C for FAU(Y) and MFI(ZSM5), respectively. Thermal gravimetric analysis (TGA) and differential scanning calorimetry (DSC) in air and N_2 atmospheres showed a thermal stability of these materials up to about 1000 °C. The catalytic activity of FAU(Y) and MFI(ZSM5) was tested by means of the cracking of 1,3,5-triisopropylbenzene (1,3,5-TIPBz) in a CREC Riser Simulator Reactor at 350 °C; the cracking of 1,3,5-TIPBz increased to about 0.6 and 1.3 times from big (108.9 and 82.8 nm) to small (18 and 20.7 nm) crystallites of FAU(HY) and MFI(HZSM5), respectively, while diffusivity increased to about 3 and 4.6 times, which demonstrates a correlation between the mean crystallite size of these zeolites with cracking activity from the external crystallite surface and the diffusivity of large reactive molecules, i.e., 1,3,5-TIPBz.

© 2010 Elsevier B.V. All rights reserved.

1. Introduction

FAU(Y) and MFI(ZSM5) zeolites are used widely in petroleum refining and petrochemicals production either as catalysts or adsorbents, i.e., FCC, aromatics alkylation, natural gas dehydration and separation media [1–5]. About 179 zeolitic materials with different frameworks have been synthesized with a wide range of pore diameters and topological networks [6]. The physicochemical properties of zeolites derive mostly from their structural char-acteristics and chemical composition, i.e., SiO_2/Al_2O_3 ratio, pore dimensions, crystal size and thickness and surface chemistry [7–9]. The synthesis of zeolites depend on several factors like the silica source, directing agent organic structure, framework elements (Ga, RE, etc.), gel composition, reaction temperature, aging time and reaction time; all these variables seem critical for obtaining a particular zeolitic structure out of several reaction pathways. In this respect, new properties of known zeolites continue to appear and keep this subject open to scientific research, as for example the recent trend on the synthesis of zeolitic crystals with a lower dimensionality, i.e., crystal sizes between 5 to about 50 nm. Nanocrystals of FAU(Y) type zeolites were reported by Mintova et al. [10,11] who synthesized colloidal crystals of FAU(Y) and LTA-type zeolites with a mean crystal size between 40 to about 80 nm, using 15-Crown-5 ether as a co-template. Holmberg et al. [12,13] reported the synthesis of small FAU(Y) crystals of about

∗ Corresponding author at: Universidad Nacional Autonoma de México, Laboratorio de Metalurgia del Instituto de Física, Apdo. Postal 20-374, 01000 México, D.F., México. Tel.: +(5255) 56225012.
E-mail addresses: pmpachec@fisica.unam.mx, pmpachec@yahoo.com.mx
(P. Morales-Pacheco).

32–120 nm diameter, which were obtained using tetramethylammonium bromide (TMABr) as a co-template. Li et al. [14] studied the nucleation and crystal growth kinetics of nanosized FAU(Y) crystallites from clear solutions, thus emphasizing the influence of the growth limiting nutrient (Na$^+$) on the crystallization process. Also, Valtchev and Bozhilov [15] made an electron microscopy study on the formation of FAU-type zeolites at room temperature. Song et al. [16] synthesized nanocrystalline FAU(NaY) with crystal sizes of 23 and 50 nm for environmental applications. Verduijn and Schoeman [17–19] reported FAU, LTA and MFI crystallites of less than 100 nm diameters. Larsen [20] reported the synthesis, characterization and applications of FAU(Y) and MFI(ZSM5) type zeolites with crystal sizes of 50 nm or less. A review of the state of the art on the crystallization mechanisms and applications of nanometric zeolite crystals was published by Tosheva and Valtchev [21].

Synthesis of nanocrystallites of MFI(ZSM5) zeolites was made by Mintova and Valtchev [22] who studied the effect of different silica sources, thus obtaining nanosized crystallites of about 15, 25 and 50 nm. Van Grieken et al. [23] reported MFI(ZSM5) crystallites of about 10–100 nm diameters, which were obtained using clear supersaturated homogeneous mixtures and a crystallization time of 24 h under hydrothermal conditions. Recently, Iwakai et al. [24] used a polyoxyethylene(15) oleyether (O-15) as a surfactant for the synthesis of MFI(ZSM5) and reported that crystal sizes decreased with the concentration of O-15, thus obtaining crystallites sizes of about 25–30 nm. Also, Aguado et al. [25] reported the synthesis and properties of MFI(ZSM5) aggregates formed by crystals of about 10–20 nm.

On the other hand the Thiele modulus (φ) is a parameter scalable down to nanometric dimensions, i.e., $\varphi = R(k_{int}/D)^{1/2}$, where R is the crystal thickness, k_{int} is the intrinsic rate constant and D is the intracrystalline diffusion coefficient. This parameter implies that thicker crystals may lead to molecular diffusion paths that are significantly longer with respect to those promoted by thin crystallites [26,27], which is accounted for the effectiveness factor, defined as $\eta = \tan(\varphi)/\varphi$, which means that the reduction of the crystallite size down to nanometric dimensions might cause a significant decrease of the molecular diffusion paths, thus improving diffusivity and reaction kinetics. The lower crystal dimensionality increases the external surface area of zeolitic crystals with respect to some amount of material composed by big crystals, i.e., 1 μm diameter thus emphasizing both surface charge effects as well as the number of accessible surface sites. Furthermore, small zeolite crystals expose a substantial fraction of their active sites on the external crystallite surface (i.e., Farcasiu and Degnan [28]) which is significant when intracrystalline diffusion limitations exist. This concept has motivated further research and some models accounting for the effectiveness of those systems have been reported for first order type reactions [28]. Thomas and Barmby [29] suggested that the primary cracking of gasoil molecules takes place first on the external surface of zeolitic crystals and, based upon this concept, Maselli and Peters [30] proposed that small crystallites may increase the whole catalytic activity for some catalytic reactions. Also, Rajagopalan et al. [31] incorporated zeolite crystallites of different sizes in a matrix and observed that the smaller crystallites were indeed more active for gasoil cracking as well as more selective towards gasoline and light cycle oil. Yamamura et al. [32] found that small MFI(ZSM5) crystals in the range 30–50 nm showed higher ethylene conversion, a higher gasoline selectivity and a lower coke yield for ethylene oligomerization with respect to conventional MFI(ZSM5) crystals. This led them to conclude that the increase of activity was due to a preferential formation of oligomers on the external crystallites surface, where more acid sites are present due to the higher external surface area. Aguiar et al. [33] found that there is no influence of the crystallite size of FAU(Y) on the cracking of n-heptane but the

cracking of 1,3,5-TIPBz proceeded at a higher conversion on small crystallites.

Therefore, the purpose of this work was to seek a correlation between the mean crystallites size and catalytic performance of nanometric FAU(Y) and MFI(ZSM5) in the cracking of 1,3,5-TIPBz. This was chosen as a model molecule because its kinetic diameter is about 0.95 nm, which is bigger than the pore diameter of FAU(Y) and MFI(ZSM5), which offers the opportunity to evaluate the external crystal surface contribution with respect to conventional zeolite crystallites.

2. Experimental

2.1. Synthesis

2.1.1. Zeolite FAU(Y)

The synthesis of FAU(Y) type zeolite nanocrystals from clear aqueous solutions with molar composition of gel: 2.4(TMA)$_2$O:0.032Na$_2$O:1.0Al$_2$O$_3$:3.4SiO$_2$:370H$_2$O was performed at 95 °C and autogenic pressure. The clear aqueous solution was obtained by dissolving tetramethylammonium hydroxide (TMAOH, Sigma) in double de-ionized water (DDI H$_2$O) and then adding aluminum isopropoxide (alumina source, 98 wt.%, Aldrich) to the alkali solution until it was dissolved completely. Then, tetramethylammonium bromide (TMABr, 98 wt.%, Fisher) and tetraethylorthosilicate (TEOS, silica source, Aldrich) were added and stirred until the solution became clear. The mix was aged during 24 h at room temperature with vigorous stirring before adding 0.4 ml of NaOH 0.1 M solution and the crystallization was started in a teflon lined stainless steel autoclave at 95 °C for a period of 144 h. Periodically, 0.4 ml of NaOH 0.1 M solution was added during the synthesis every 12 h, until obtaining a gel with the following composition 2.4(TMA)$_2$O:0.43Na$_2$O:1.0Al$_2$O$_3$:3.4SiO$_2$:370H$_2$O.

2.1.2. Zeolite MFI(ZSM5)

The MFI(ZSM5) type zeolite nanocrystals were synthesized with the following gel molar composition: 9.12(TPA)$_2$O:60SiO$_2$:0.5Al$_2$O$_3$:936H$_2$O. The main chemical precursors were aluminum sulfate (Al$_2$(SO$_4$)$_3$·18H$_2$O, J.T. Baker) and fumed silica (CAB-O-SIL)), which were combined within a boiling solution of de-ionized water with tetrapropylammonium hydroxide (TPAOH, Aldrich). After 10 min stirring under reflux a clear homogenous solution was obtained, which was cooled down to room temperature, while the mass losses were compensated by adding DDI H$_2$O. The clear solutions were stored into flasks, which were fitted with reflux condensers in oil bath. The crystallization took place at atmospheric pressure (i.e., 582 mm Hg in Mexico City) under static conditions, at 80 °C; the product was analyzed after 216 h of crystallization and calcined at 550 °C.

In both synthesis procedures the materials were washed and dispersed in DDI H$_2$O, then were centrifuged at 2×10^4 rpm for 50 min, in order to separate the solid phase and then were re-dispersed in DDI H$_2$O again, using an ultrasonic bath; this process was repeated 3 times, then the materials were dried at 110 °C during 12 h and then calcined at 550 °C during 4 h till elimination of the organic template. Afterwards, the zeolitic materials were ion-exchanged with a solution of 1 M of NH$_4$NO$_3$ (3 h and 25 °C) and then washed with DDI H$_2$O and calcined at 550 °C for elimination of the NH$_3$, thus obtaining zeolitic nanocrystals in acidic form, i.e., FAU(HY) and MFI(HZSM5). The crystalline materials were studied by X-ray diffraction (XRD) in a Siemens D5000 diffractometer ($\lambda_{Cu} = 0.1541$ nm), in the 2θ range 4–50°. The mean size of the crystals was measured by Rietveld's method using Scherrer's equation [34,35] and also the crystallites size was verified by TEM.

The HRTEM was made using the FEI (TECNAI) FE30 (300 kV) and JEOL (200 kV) 2200 FS microscopes, where the calcined samples were mounted onto copper grids. HRTEM computer simulations were performed according to the multislice approach pioneered by Cowley and Moodie [36] which is included in the HRTEM module of the Cerius^2 interface [37]. Cerius^2 is a molecular simulator from Accelrys Inc. The multislice method is used for electron microscopy image simulations with the following sequence: (a) the crystal potential is divided in slices and then projected on a plane perpendicular to the direction of the electron beam; (b) a planar incident electron wave-front interacts with the first plane followed by the calculation of the scattered beams; (c) propagation of the (scattered) beams through vacuum and (d) interaction of the beams with the next plane. The simulated images were compared with the experimental ones using standard image processing methods (Digital Micrograph Program from Gatan Inc.).

The surface characterization of the samples was performed by FTIR spectroscopy using an Infrared Nicolet spectrophotometer (Model Magna 560) with the samples diluted in KBr (spectroscopy grade). The surface acid type distribution was determined by FTIR of adsorbed pyridine. All the spectra were recorded at intervals of about 4 cm^{-1}. The samples were finely ground and pressed into a self-supporting wafer (8–10 mg/cm^2, diameter = 15 mm), which were placed into an infrared cell with KBr windows. A previous evacuation at 500 °C (ca. 10^{-4} Torr) for 4 h was carried out before introducing pyridine. The IR spectra were recorded after subsequent evacuation at increasing temperatures from 25 to 400 °C (1 h at each temperature). The pyridine concentrations in the Bronsted (B) and Lewis (L) type acid sites is obtained by the following equations [38]:

$$C\,(\text{pyridine on B sites}) = \frac{1880 A_I(B)\,R^2}{W};\qquad(1)$$

$$C\,(\text{pyridine on L sites}) = \frac{1420 A_I(L)\,R^2}{W}.\qquad(2)$$

These equations ((1) and (2)) are obtained starting from the integrated molar extinction coefficient (IMEC, Eq. (3)) and the Beer's law (Eq. (4)).

$$\text{IMEC} = \int \varepsilon\,d\sigma \qquad(3)$$

$$A = \varepsilon c D \qquad(4)$$

where C is the concentration (μmol/g catalyst), $A_I(B,L)$ the integrated absorbance of B or L band (cm^{-1}), R the radius of sample disk (cm), W the weight of disk (mg), σ the wavenumber (cm^{-1}), A the absorbance = $\log_{10}(I_0/I)$, where I_0 and I are the intensities of incident and transmitted radiation, ε the molar extinction coefficient (dm^3/(mol cm)), c the concentration (mol/dm^3), and D is the path length (cm).

Nitrogen adsorption measurements were carried out at 77 K on an ASAP 2010 automatic adsorption analyzer fitted with the micropore options from Micromeritics. Before measurements, the samples weighing about 0.1–0.3 g were placed in the degassing port of the adsorption apparatus for degassing at 100 °C for 1 h and at 300 °C for 10 h. The data from the low-pressure region were obtained by contacting the sample with successive increments of the nitrogen (doses of 3 cm^3/g STP of sample) and waiting until thermal equilibrium was reached. Adsorption isotherms were measured under the relative pressure range (P/P_0) based upon the saturation vapor pressure, from ~10^{-6} to 1.

TGA and DSC were carried out on a Perkin Elmer Thermogravimetric analyzer model TGA-7HT at a heating rate of 10 °C/min in air and N$_2$ atmosphere. These methods were useful to determine the thermal stability of the nanocrystalline materials.
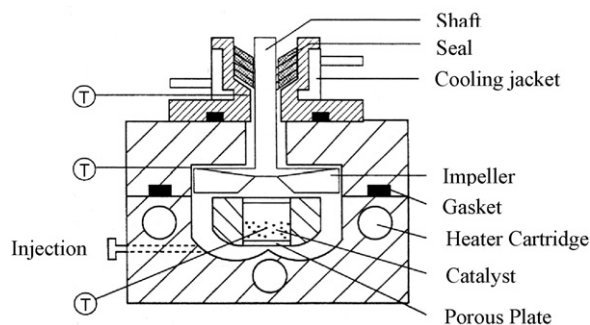

Fig. 1. Schematic representation of the CREC Riser Simulator Reactor [40].

The catalytic activity of both FAU(HY) and MFI(HZSM5) was carried out using samples of the zeolites with different crystal sizes; the 1,3,5-TIPBz kinetic diameter in 0.95 nm [39] which is bigger than the pores entrance of both zeolites, i.e. 0.74 nm for FAU(Y) and 0.56 nm for MFI(ZSM5). The CREC Riser Simulator Reactor is a novel bench scale reactor with an internal recycle unit. It consists of two outer shells, where the lower and upper sections permit the loading or unloading of the catalysts (Fig. 1) [40]. This reactor was designed in such a way that an annular space is created between the outer portion of the basket and the inner part of the reactor shell. A metallic gasket seals the two chambers and there is an impeller located in the upper section. A packing gland assembly and a cooling jacket surround the shaft supports of the impeller. Upon rotation of the shaft, gas is forced outwards from the center of the impeller towards the walls, which creates a pressure in the central region of the impeller, thus inducing the gas flow upwards through the catalyst chamber from the bottom of the reactor (annular region) where the pressure is slightly higher. The impeller provides a fluidized bed of catalyst particles as well as an intense gas mixing inside the reactor. The CREC Riser Simulator Reactor operates in conjunction with a series of sampling valves that allow following a predetermined sequence, the injection of hydrocarbons and the withdrawal of products in short periods of time. The reaction products were measured by a Hewlett Packard 5890A Gas Chromatograph with a flame ionization detector (FID) and a HP-1, 30 m capillary column of cross-linked methyl silicone, with an outer diameter of 0.20 mm and an internal diameter of 0.3 μm. The experimental test conditions are shown in Table 1.

The diffusivity of 1,3,5-TIPBz in the zeolite was estimated by means of a graphical method [41] (Fig. 2) and using the kinetic data obtained by cracking of 1,3,5-TIPBz at 350 °C over FAU(HY) and MFI(HZSM5) catalyst, which had identical Si/Al ratio and crystallinity percentage, but different crystallite sizes (i.e. 18.4 and 108.9 nm for the FAU(Y) and 20.7 and 82.8 nm for MFI(ZSM5)). The kinetic data on these two different sets of crystals sizes were obtained by conducting the reaction over a range of contact times, i.e., the rate constants K_{obs} were obtained from the slopes of first order plots of conversion versus contact times. This method gives

Table 1
Test conditions in the cracking reaction of 1,3,5-triisopropylbenzene in a CREC Riser reactor simulator.

Mass of catalyst (g)	0.10
Feed	1,3,5-Triisopropylbenzene (1,3,5-TIPBz)
Density of feeding (g/cm^3)	0.854
Volume of feed of 1,3,5-TIPBz (cm^3)	0.20
Mass of feed: 1,3,5-TIPBz (g)	0.17
Mass catalyst/mass 1,3,5-TIPBz (g/g)	0.59
Reaction temperature (°C)	350
Reaction time (s)	3, 6, 9 and 12
Reactor volume (l)	0.047
Nitrogen flow (cm^3/min)	110

Fig. 2. Log scale plot of η versus φ [41].

Fig. 3. X-ray powder diffraction patterns of zeolitic materials: (a) FAU(Y) zeolite and (b) MFI(ZSM5) zeolite. Arrows show the high index planes.
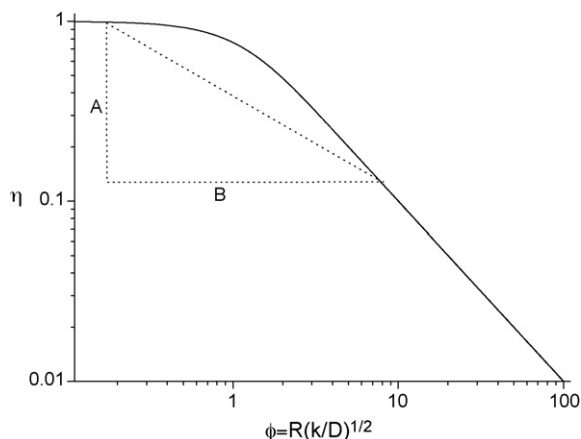
also the effectiveness factor (η) and the Thiele modulus (φ). The calculation of these parameters let us observe the correlation of the kinetic and diffusion parameters with the crystallites sizes.

3. Results

3.1. Structural properties

Fig. 3a and b shows the XRD patterns of FAU(Y) and MFI(ZSM5); in both cases the typical features (i.e. peak intensities and angular (2θ) positions) correspond to the ones found in conventional zeolites [42,43], thus revealing the presence of a single crystalline phases, where the preferential orientation of the crystallites are along the plane (1 1 1) for FAU(Y) and (0 1 1) for MFI(ZSM5). Arrows in both figures show the high index planes, which indicate the complex planes presents in these crystallites.

3.1.1. FAU(Y)
The nanometric dimensions of FAU(Y) type zeolite crystals were verified by HRTEM in the size range between 20 and 40 nm, as shown in Fig. 4a. A typical experimental image corresponding to a FAU(Y) crystallite viewed along ⟨1 0 1⟩ axis is illustrated in Fig. 4b. One observes the ordered arrays of pores with a cubic symmetry and pore diameter of about 0.74 nm, which are the typical features of the pore system reported for FAU(Y) type zeolites [44]. Fig. 4c and d displays the experimental and simulated optical transforms of a FAU(Y) crystal slab corresponding to a perfect model, with $\Delta F = +60$ nm, Cs = 0.5 mm, $\varphi = 0$ and four unit cells depth. In general, the crystallites have an external cubic habit and crystallite sizes in the range between 20 and 40 nm; these results coincide with the previous Rietveld's analysis. In addition, a sequence of the simulated HRTEM images was calculated in function of intrinsic and instrumental parameters, such as defocus (ΔF), the angle of deviation (φ) from the zone axis ⟨1 0 1⟩, the number of zeolite cell units (depth along ⟨1 0 1⟩ axis) and the spherical aberration coefficient (Cs). These theoretical calculations were carried out using the HRTEM module implemented in the Cerius^2 interface. A comparison between the experimental and theoretical lattice images is shown in Fig. 5 for crystals of FAU(Y) zeolite in the range between 20 and 40 nm; a contrast variation around the pores is observed, i.e., it passes from black to white along certain directions, which may be due to local thickness variations, distinct tilting angles and some instrumental factors (aberrations, defocusing) mainly; it also shows a contrast inversion between some regions of different crystals (i.e., in Fig. 5a, the crystal shown in the upper left hand side with respect lower right hand side), which is verified as a contrast difference between pores having white and black contrast. Fig. 5b corresponds
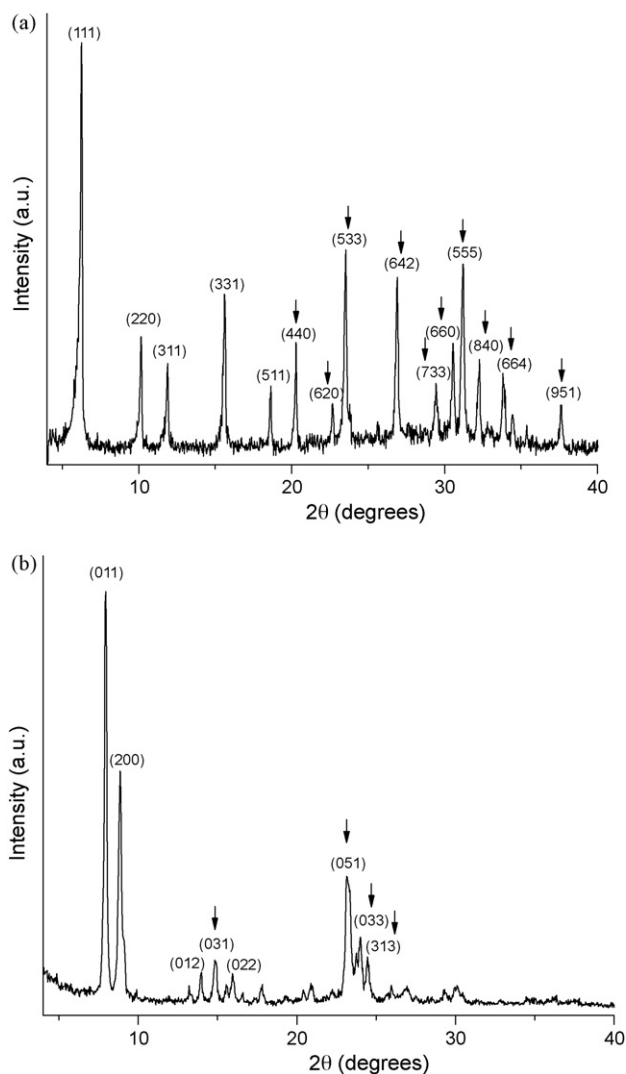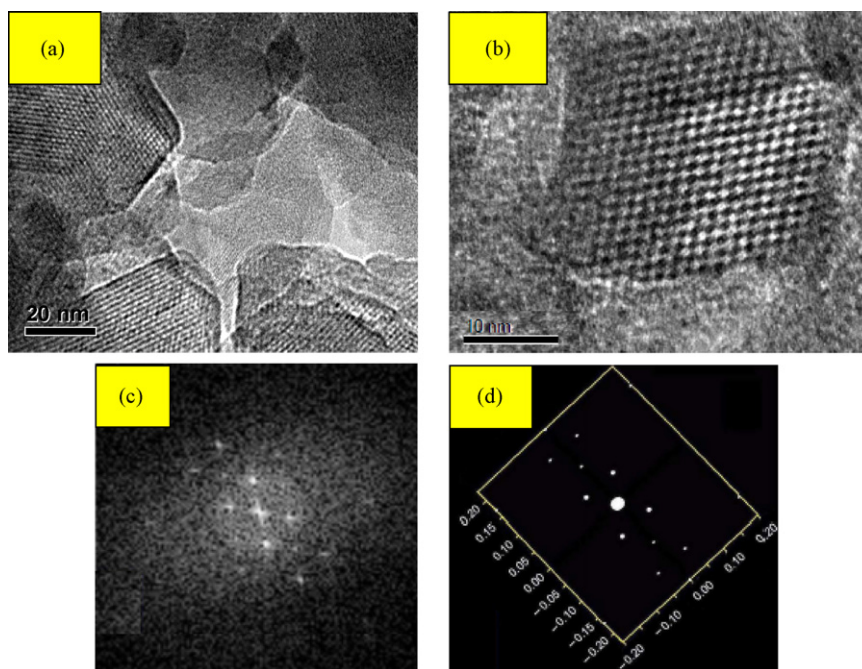
to a HRTEM image of a zeolite FAU(Y) type crystal, whose pores array is viewed perpendicularly to the (1 0 1) plane, which coincide with the zeolite FAU(Y) theoretical projection along ⟨1 0 1⟩. Fig. 5c displays the superposition of theoretical crystalline pore arrays corresponding to FAU(Y) (1 0 1) plane over the experimental HRTEM image of the nanosized zeolite FAU(Y). Fig. 5d illustrates the theoretical crystalline array of the plane (1 0 1). Fig. 5e shows the HRTEM simulated image of a four-cells depth crystal slab model of zeolite FAU(Y) with zone axis ⟨1 0 1⟩, $\Delta F = +60$ nm, Cs = 0.5 mm, $\varphi = 0$. On Fig. 5f one observes the atomic position of the basic unit cell used for comparison.

3.1.2. MFI(ZSM5)
Figs. 6 and 7a display the TEM images of different regions corresponding to MFI(ZSM5) with two orientations of the small crystallites, i.e., Fig. 6 and region A of Fig. 7a show a crystalline domain exposing the (0 1 0) plane perpendicular to the observation axis. Also, Fig. 7a shows region B, which corresponds to a stack of crystallites with sizes between 20 and 40 nm diameters viewed along the [0 0 1] "edge-on" direction. The crystalline domains in region B are about 30 nm diameter, whose boundaries are clearly outlined. Also in Fig. 7a the region A shows the nanocrystals embedded in the aluminosilicate matrix and the typical rounded outline

Fig. 4. (a) Crystals of FAU(Y) zeolite in the size range between 20 and 40 nm, (b) HRTEM image of a single zeolite crystal after 144 h of crystallization, (c) optical transform of (b), and (d) is a simulated optical transform of a slab model of zeolite FAU(Y), having four unit cells depth and zone axis $\langle 1\,0\,1\rangle$, $\Delta F = +60$ nm, Cs = 0.5 mm, $\varphi = 0$.
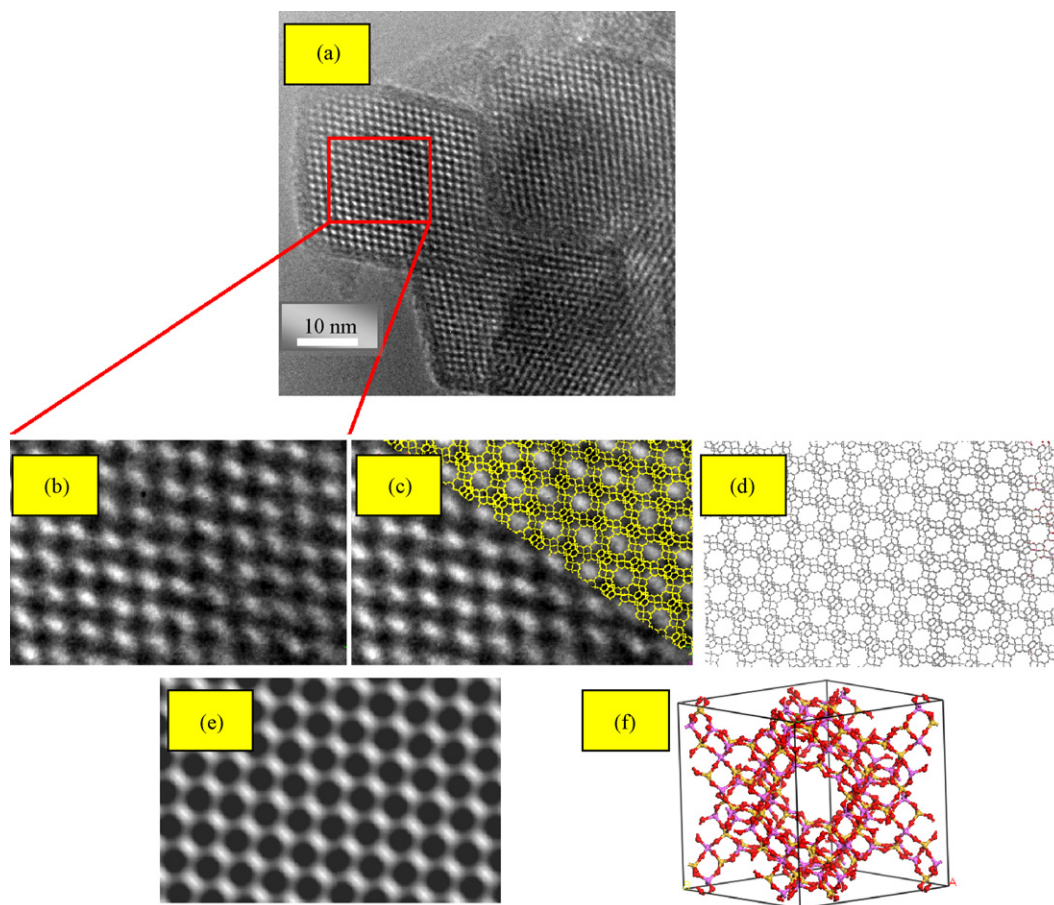
Fig. 5. (a) Typical crystals of FAU(Y) zeolite in the size range between 20 and 40 nm, and (b) HRTEM image of zeolite $(1\,0\,1)$-FAU(Y). (c) Superposition of the $(1\,0\,1)$ plane over the experimental HRTEM image of nanocrystalline FAU(Y), i.e., after 144 h crystallization. (d) Theoretical grid of FAU(Y) structure viewed along the zone axis $\langle 1\,0\,1\rangle$. (e) HRTEM simulation image of a four unit cells depth slab model of FAU(Y) with zone axis $\langle 1\,0\,1\rangle$, $\Delta F = +60$ nm, Cs = 0.5 mm, $\varphi = 0$, and (f) basic cell of FAU(Y) with cell dimensions $a = b = c = 2.474$ nm.
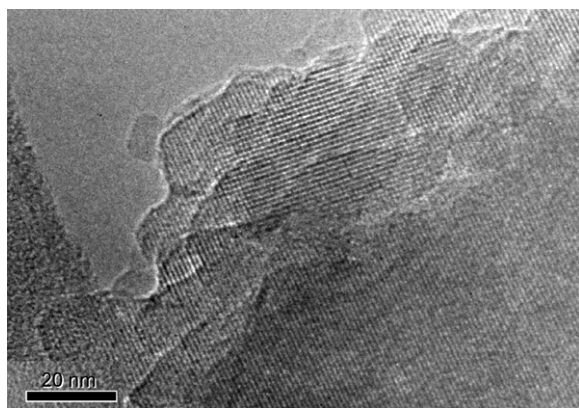
Fig. 6. TEM micrographs showing a typical aggregate of MFI(ZSM5) crystallites laying on the (0 1 0) face.

with irregular rims; in this case the typical crystallite sizes are in the range between 20 and 40 nm diameters; the crystalline aggregates of region B have a diameter of about 60 nm. Also, Fig. 7b shows an expanded view of a section of region A, from which one observes clearly the symmetry of the inner pore arrays and the pore dimensions, that confirms the MFI(ZSM5) type structure oriented perpendicularly to the [0 1 0] crystal axis, i.e., the symmetry corresponds to the space group Pnma and the mean pore diameter is equal to 0.56 nm [45–47]. The experimental and calculated optical transforms are shown in Fig. 7c and d, respectively, which

confirm the crystallite orientation perpendicular to *b* axis (region A) as well as the alternate orientation of the stacks of crystallites corresponding to region B.

A series of simulated HRTEM images was calculated using the kinematical approach and the results are displayed in Fig. 8. Fig. 8a shows one crystal of MFI(ZSM5) with a size of about 30 nm, where one observes the contrast variation around the pores, which passes from black to white along certain directions due to a local thickness variation, tilting and instrumental factors (aberrations, defocusing). One observes a contrast inversion between the different zones due to contrast differences between white and black pores. Fig. 8b is an expanded view of the experimental image showed in Fig. 8a, where a typical MFI(ZSM5) crystallite is laying on (0 1 0) plane. Fig. 8c illustrates the superposition of the theoretical structural model over the experimental HRTEM image of [0 1 0]-MFI(ZSM5). Fig. 8d corresponds to the crystalline grid, i.e. the atomic potential image. Fig. 8e shows the simulated image of a MFI(ZSM5) crystal for a thickness (*t*) equivalent to 3 unit cells (5.970 nm), $\Delta F = 0$, $\varphi = 0$. Finally Fig. 8f corresponds to the basic cell of MFI(ZSM5).

3.2. Surface properties

Fig. 9a and b displays the IR absorption bands which are typical of both symmetrical and non-symmetrical C–H and Si–O vibrations, appearing on the high energy region from 1500 to 4000 cm^{-1}, while the low-energy bands in Fig. 9a and b (inset) are assigned to bond deformations [48–50]. There one observes the typical stretching bands of water around 3420 to 3460 cm^{-1} together with shoulders in this region that indicate the presence of structural OH groups.
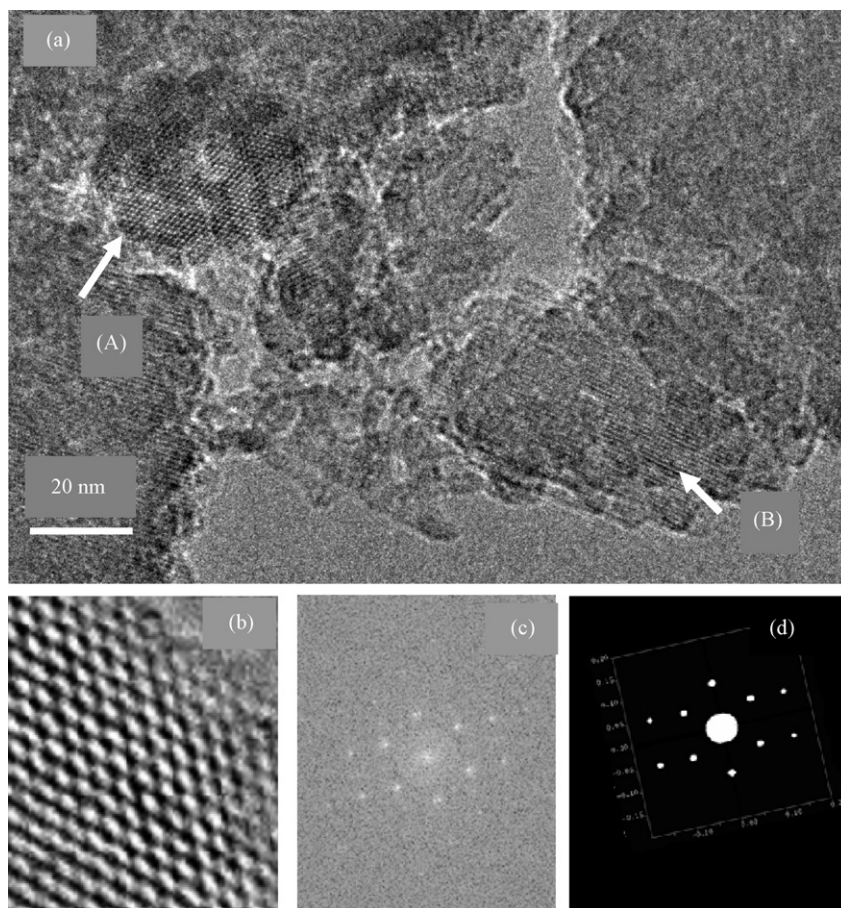
Fig. 7. (a) HRTEM image of MFI(ZSM5). Region A is a ⟨0 1 0⟩ oriented crystallite and region B is a stack of crystallites viewed along ⟨0 0 1⟩ direction. (b) Expanded view of a section of region A above showing the typical inner pore array. (c) Optical transform of region A, and (d) Simulated optical transform of a slab model for MFI(ZSM5) corresponding to three unit cells depth and zone axis ⟨0 1 0⟩.
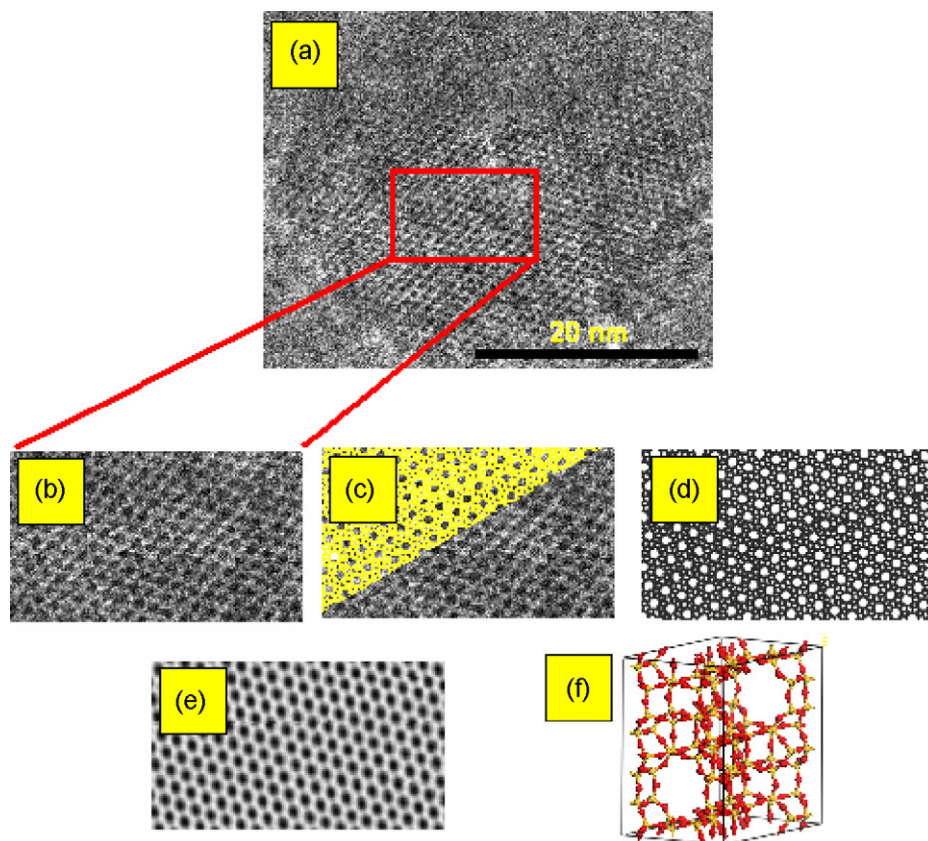
Fig. 8. (a) MFI(ZSM5) crystallite with a size of about 30 nm, (b) Experimental HRTEM micrograph of (0 1 0)-MFI(ZSM5). (c) Superposition of the crystalline atomic model over the experimental HRTEM image of (0 1 0)-MFI(ZSM5). (d) Crystalline grid (atomic model) of MFI(ZSM5). (e) Simulated image of the MFI(ZSM5) crystal for a thickness (t) equivalent to 3 unit cells (5.970 nm), $\Delta F = 0$, $\varphi = 0$. (f) Basic cell of MFI(ZSM5) with cell dimensions $a = 2.0022$ nm, $b = 1.9899$ nm and $c = 1.3383$ nm.

The band at about 1620 to 1640 cm^{-1} is assigned to a scissor-type vibration band arising from the proton vibration in the water molecules [48–50]. The bands at 1250–950 cm^{-1} are assigned to asymmetrical stretching vibrations corresponding to the tetrahedral Si, Al atoms [48–50]. The band between 810 and 700 cm^{-1} is assigned to Si–O symmetrical stretching vibrations, while the band occurring at 550 to 555 cm^{-1} arises from the presence of structural double D6R rings in the case of FAU(Y) zeolite (Fig. 9a), while there is a sharper and more intense band in the case of MFI(ZSM5), however in the latter case the band arises from structural double D5R rings [48–50] (Fig. 9b). This band is important in both materials because it is sensitive to the crystalline nature of the solids [48,49], as indicated in Fig. 9a and b. The band appearing between 465 and 455 cm^{-1} can be assigned to the structure-insensitive internal tetrahedral bending bond, i.e., T–O$_4$ (T: Si or Al) [48].

The surface acidity of the solids was also determined by FTIR of adsorbed pyridine over the surface of FAU(Y) after 144 h crystallization. Fig. 10a and b shows the results of both as-synthesized and NH$_4$NO$_3$-exchanged, with further calcination (acid form), respectively. One observes the presence of five bands where the first appears at 1443 cm^{-1}, which is due to the bond of pyridine (adsorbed) and surface Lewis type sites. Secondly, the band at 1490 cm^{-1} arises more probably from a combination of Bronsted and Lewis type sites; the band at 1540 cm^{-1} arises from the pyridinium ion formed on a Bronsted type site [51], while the band at 1596 cm^{-1} probably belongs to a Lewis type site. Also, one observes that the band at 1443 cm^{-1} shows a double signal up to about 100 °C which is due to the interaction of pyridinium ion with neutral hydrogen from adsorbed water, furthermore, the band appearing at 1640 cm^{-1} (i.e., at 25 °C) arises more probably from a combi-

nation of Brönsted and Lewis acid sites; the spectrum obtained at 100 °C shows more clearly a doublet formed by two bands, one at 1635 cm^{-1}, which can be assigned to the interaction of pyridinium ion from a Bronsted type site with neutral hydrogen from adsorbed water, and the band at 1615 cm^{-1} that probably belongs to pyridine adsorbed physically on Lewis type sites. In the case of the as-synthesized nanometric FAU(Y) materials the FTIR bands are present up to about 200 °C but, in the acid type material FAU(HY) these bands withstand temperatures up to about 400 °C, which indicates a higher acid strength with respect to the as-synthesized FAU(Y) [51,52].

Fig. 10c and d shows the FTIR spectra of adsorbed pyridine on the surface of the nanocrystals of MFI(ZSM5) zeolite, both as-synthesized and NH$_4$NO$_3$-exchanged, with further calcination (acid form). One observes that the as-synthesized and calcined materials do not show the presence of Brönsted acid sites while the bands arising from Lewis acid type sites (i.e., 1443, 1490 and 1596 cm^{-1}) remain up to about 100 °C, which is caused more probably by neutral hydrogen that comes from absorbed water. For the acidic materials MFI(HZSM5) these bands remain up to about 400 °C, thus indicating the higher acid strength with respect to the as-synthesized materials MFI(ZSM5). Furthermore, for acid materials there appears a partition of the band at 1645 cm^{-1}, which shows that at 100 °C there appears a double signal, one appearing at 1640 cm^{-1} from the interaction of pyridinium ion with Bronsted type sites, while the band at 1615–1620 cm^{-1} belongs more probably to Lewis type sites.

In contrast, FAU(Y) zeolite shows a higher intensity for both sets of acid bands with respect to the bands shown by MFI(ZSM5), thus indicating that Y zeolite has a greater number of acid sites (i.e., see Tables 2 and 3). This behavior may be due to the higher amount
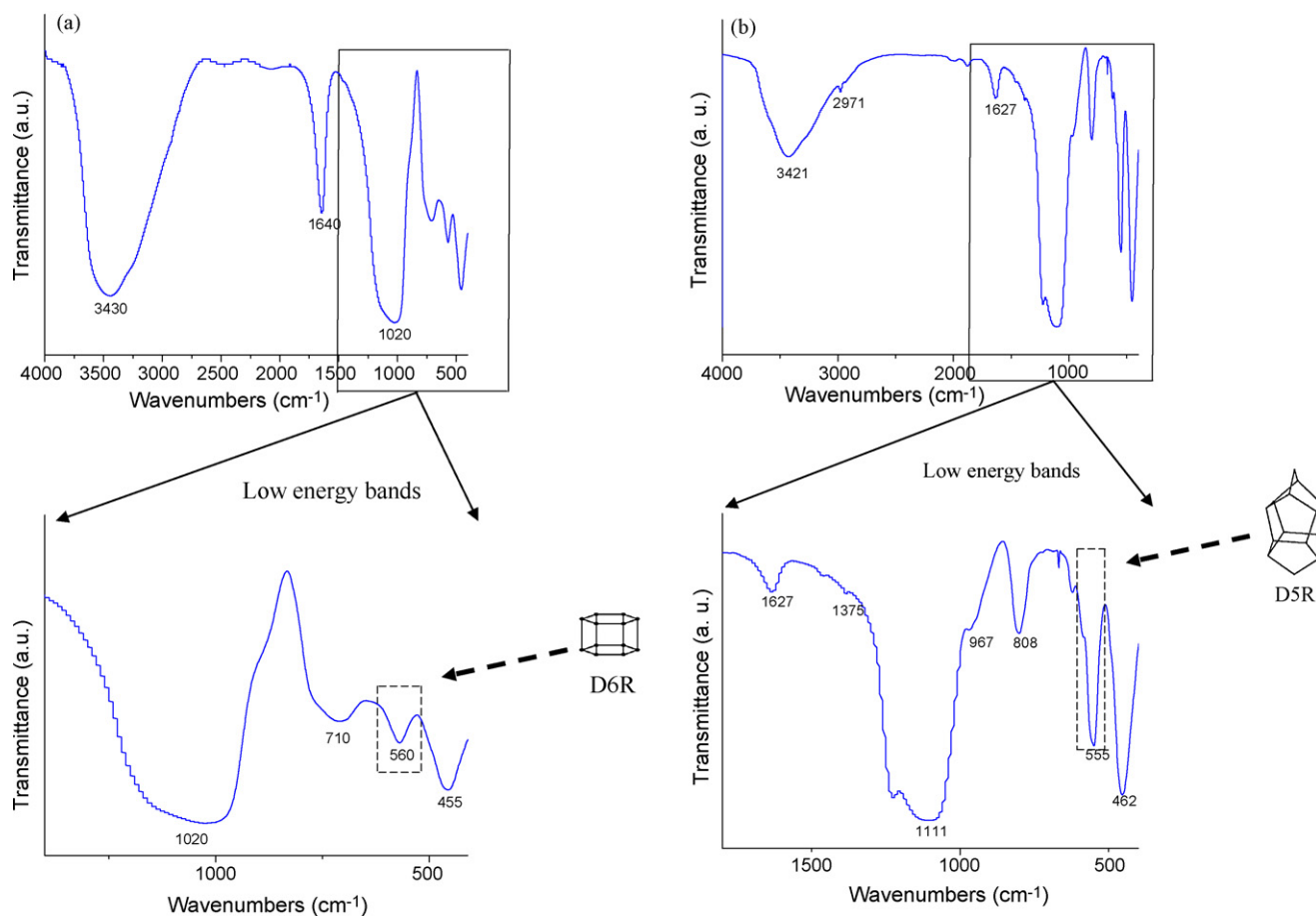
Fig. 9. FTIR (KBr) spectra of the as-synthesized zeolites. An expanded view of the lower frequency region is included in both cases, with the main crystallization bands encircled. The dotted arrow indicates the position of this crystallization band, at 555–560 cm^{-1}, which is assigned to the presence of structural double rings of (a) D6R for FAU(Y) zeolite, and (b) D5R for MFI(ZSM5) zeolite.

Table 2
Surface acidity of nanosized crystals of FAU(Y) after 144 h crystallization (μmol(Py)/g (cat)).

Temperature (°C)	FAU(NaY)			FAU(HY)		
	Brönsted	Lewis	Total acidity (B + L)	Brönsted	Lewis	Total acidity (B + L)
25	81	418	499	191	999	1190
100	96	99	195	180	396	576
200	60	81	141	170	36	206
300	9	59	68	95	45	140
400	0	54	54	72	12	84

of structural aluminum (i.e., Al^{IV} or a small Si/Al ratio) in FAU(Y) zeolite.

Also the surface texture of the nanometric materials was characterized by means of N$_2$ adsorption–desorption (BET) isotherms as shown in Fig. 11a and b. For FAU(Y) zeolite (Fig. 11a) the initial adsorption step at low relative pressure indicates a complete filling of the micropores. The hysteresis loop of the isotherm is in the range of relative pressures from 0.50 to 1.0, which strongly

suggests the formation of mesopores. The as-synthesized FAU(Y) zeolite nanocrystals prepared in batch, exhibited a BET surface area of 658 m^2/g, a mesopore volume (V_P) of 0.85 cm^3/g (i.e., this parameter was determined by the t-plot method) and the mean mesopore diameter (D_P) of 4.2 nm (i.e., this parameter was determined by BJH's method). These numbers are higher than the ones obtained for commercial materials (Zeolyst CBV720 series), i.e., S_{BET} = 619 m^2/g, V_P = 0.38 cm^3/g and D_P = 1.8 nm.

Table 3
Surface acidity of nanosized crystals of MFI(ZSM5) after 216 h crystallization (μmol(Py)/g (cat)).

Temperature (°C)	MFI(ZSM5) (as-synthesized)			MFI(H-ZSM5)		
	Brönsted	Lewis	Total acidity (B + L)	Brönsted	Lewis	Total acidity (B + L)
25	0	1058	1058	125	959	1084
100	0	123	123	124	70	194
200	0	0	0	86	33	119
300	0	0	0	43	31	74
400	0	0	0	11	23	34
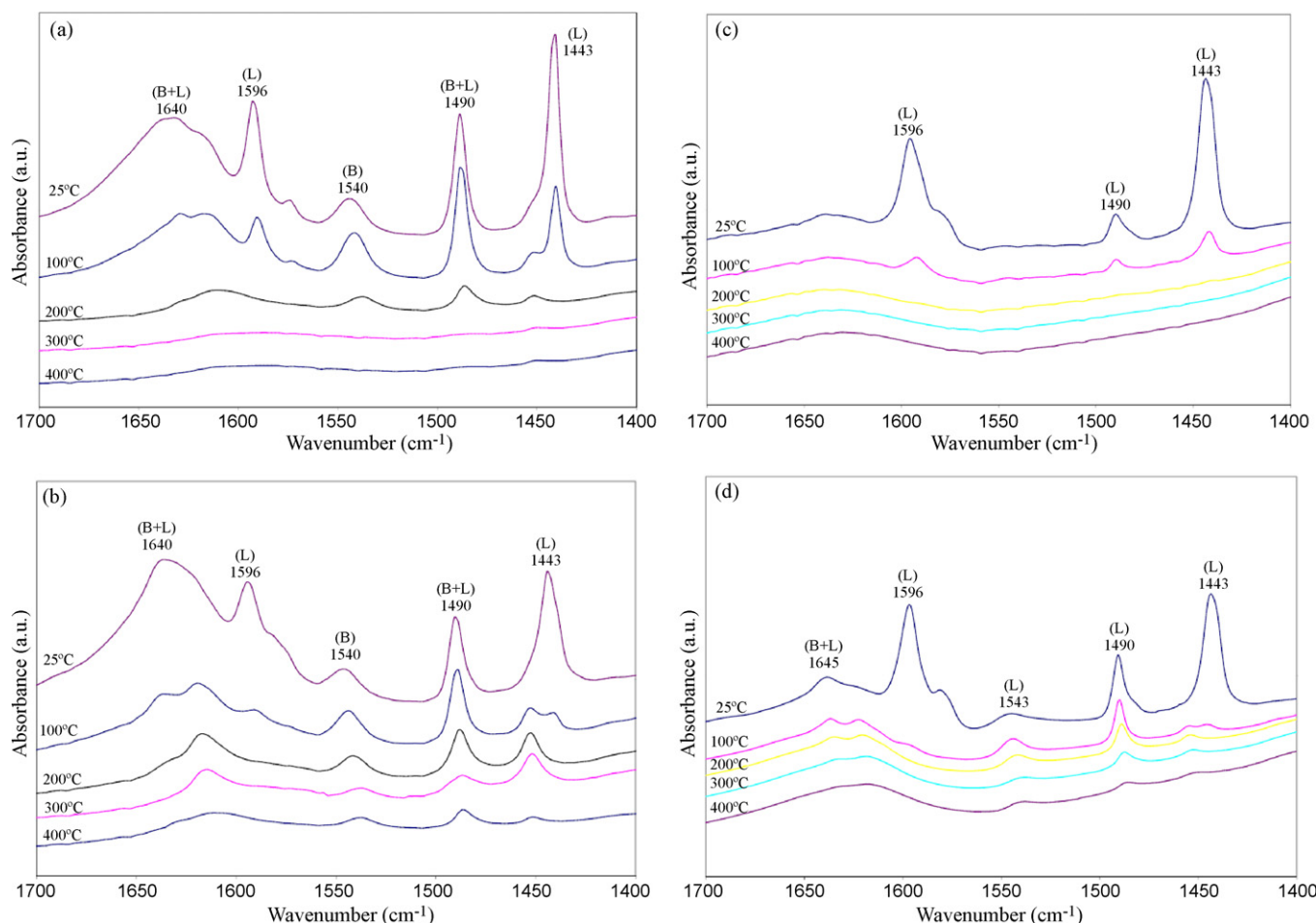
Fig. 10. Pyridine adsorption on nanocrystalline materials: FAU(Y) zeolite (a) as-synthesized, (b) acid form and, MFI(ZSM5) (c) as-synthesized and, (d) acid form. Lewis acid sites (L) and Brönsted acid sites (B) are marked.

Fig. 11b shows that MFI(ZSM5) presents an initial adsorption step at a low relative pressure, which indicates a complete filling of the micropores. The hysteresis loop of the isotherm, in the range of relative pressure from 0.40 to 1.0, strongly suggests the formation of mesopores. The as-synthesized zeolite MFI(ZSM5) nanocrystals (i.e., which were synthesized in a batch mode) exhibited a BET surface area of 495 m^2/g, a mesopore volume of 0.39 cm^3/g (i.e., this parameter was determined by the t-plot method) and a mean mesopore diameter of 2.4 nm (i.e., from BJH's method). These figures are higher than the ones obtained for commercial materials (Zeolyst CBV-1502 series), i.e., S_{BET} = 434 m^2/g, V_P = 0.23 cm^3/g and D_P = 2.1 nm.

3.3. Thermal properties

Fig. 12a shows the TGA thermograms of nanometric FAU(Y) in N$_2$ and air atmosphere; there is a 22.1% loss in weight with N$_2$ from room temperature to 200 °C, a 2.0% loss in weight between 200 and 1000 °C. On air atmosphere there is a 21.8% loss in weight and 1.8% loss into the same intervals, respectively. The DSC analysis is illustrated in Fig. 12b which does not present any transition in both inert and oxidative atmosphere for FAU(Y), which let us conclude that this material is thermally stable.

Fig. 12c shows the TGA thermograms on N$_2$ and air atmospheres for MFI(ZSM5); there is a 7.9% loss in weight in N$_2$ from room temperature to 200 °C, and 1.7% loss from 200 to 1000 °C while TGA analyses on air atmosphere revealed a 7.6% loss and 1.3% loss in the

same interval. Fig. 12d shows the DSC analysis which presents a transition at 203.4 °C in N$_2$ while this transition occurs at 190.9 °C in air. This behavior shows that this material is thermally stable. In both cases the weight loss from room temperature to 200 °C is due to moisture adsorbed by these materials from the environment and the subsequent weight loss is probably due to residual organic material.

3.4. Catalytic properties

The measurement of catalytic activity should lead to some effects caused by differences of the crystallite size of FAU(Y) and MFI(ZSM5) zeolites, specially from those related to the active sites population on the outer crystal surface, which should increase with the diminution of the zeolite crystal size.

In general, the 1,3,5-TIPBz conversion increased with the reaction time (3–12 s) for all the materials composed by nanosized crystals, except the case of big MFI(ZSM5) big crystals (i.e., into the interval 9–12 s).

Fig. 13a and b shows the increase of 1,3,5-TIPBz cracking with a diminution of the zeolite crystallite size at about or similar SiO$_2$/Al$_2$O$_3$ ratios. Fig. 13a illustrates the typical results obtained for FAU(Y) in function of the mean crystal size, thus for small crystal sizes a higher 1,3,5-TIPBz cracking was verified with respect to the other crystal sizes; for big and medium crystal sizes the conversion of 1,3,5-TIPBz was similar until 9 s reaction time, afterwards, for the bigger crystallites the conversion of 1,3,5-TIPBz is
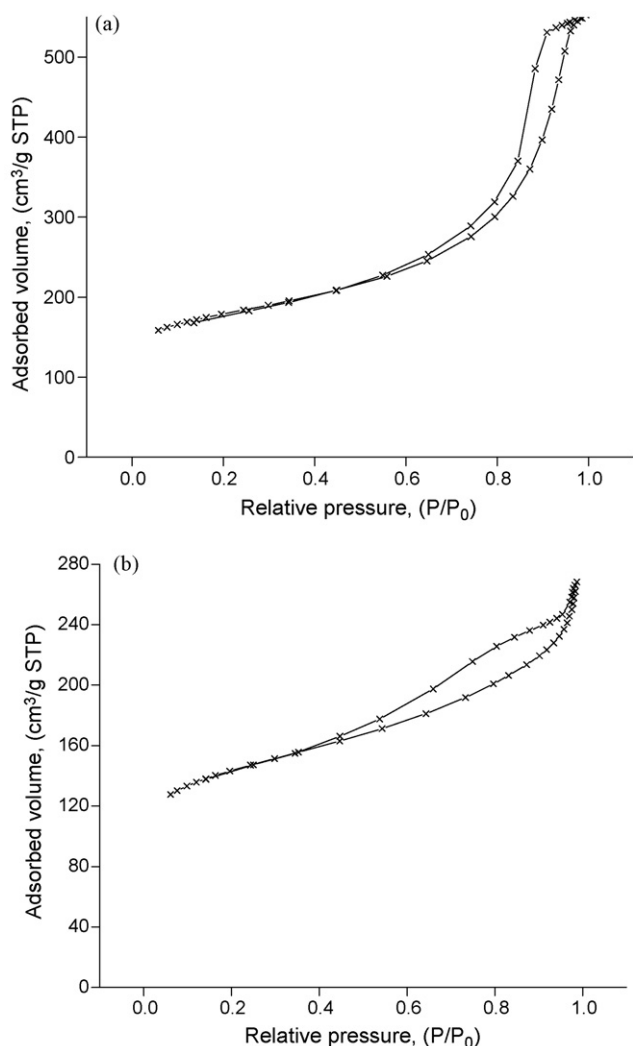
Fig. 11. N$_2$ adsorption–desorption isotherm of as-synthesized materials: (a) FAU(Y) and (b) MFI(ZSM5).

still increasing, at a rate lower than medium crystallites (Fig. 13a), while small crystallites show an increasing conversion with time of reaction. Also, Fig. 13b shows that for MFI(ZSM5) the conversion for small and medium crystal sizes was similar at the beginning but it was diverging with the reaction time; in both cases the 1,3,5-TIPBz cracking increased after 9 s while the crystal sizes decreased, this was probably due to accumulation of coke on the catalysts surface. The overall conversion of 1,3,5-TIPBz was higher for FAU(Y) with respect to MFI(ZSM5); in both cases the slope increased after 9 s of reaction except for bigger crystals of MFI(ZSM5). However in all cases the conversion of 1,3,5-TIPBz was higher on the materials containing small crystallites.

4. Discussion

The main structural features of the nanometric FAU(Y) and MFI(ZSM5) were verified by means of XRD patterns and high resolution electron microscopy. The XRD results indicate the formation of crystalline materials with high index planes. The nanocrystals of FAU(Y) showed a well-defined profile with a cubic morphology and a mean crystal size varying between 20 and 40 nm, in agreement with Rietveld's analysis. The rhombic symmetry of the pore arrays in FAU(Y)'s nanocrystals corresponded to the (1 0 1) surface array of conventional FAU(Y) and the simulated image from

a slab model of FAU(Y) corresponded to a four unit cell depth crystal with a zone axis $\langle 1\,0\,1 \rangle$, $\Delta F = +60$ nm, Cs = 0.5 mm, $\varphi = 0$. The superposition of simulated images of a FAU(Y) slab model over the experimental HRTEM images along the zone axis $\langle 1\,0\,1 \rangle$ illustrated the coincidence between the experimental and the simulated images.

The nanocrystals of MFI(ZSM5) showed a disk-like morphology, which might be the result of an almost quasi 2D crystal growth in isotropic conditions. The rounded shapes of the crystallites rim indicate the presence of high index planes, which coincides with the XRD results.

The FTIR with KBr study indicated that the absorption bands corresponded to typical IR spectra of FAU(Y) and MFI(ZSM5). In particular, the band at 555–560 cm^{-1} was assigned to double rings (D6R) block vibrations for FAU(Y) and double rings (D5R) block vibrations for MFI(ZSM5); in both cases this band is sensitive to the crystalline nature of those materials, i.e. the band intensity increases with crystallinity. Also, the FTIR spectra of adsorbed pyridine on the nanosized crystallites of FAU(Y) showed five bands appearing at 1443 cm^{-1}, 1490 cm^{-1}, 1540 cm^{-1}, 1596 cm^{-1} and 1640 cm^{-1}. For FAU(Y) the bands appearing at 1443 cm^{-1}, 1490 cm^{-1} and 1596 cm^{-1} correspond to pure Lewis type sites, in the first and third case, and to a combination of Lewis and Bronsted type sites in the other case. The band at 1540 cm^{-1} arises from Bronsted type sites exclusively. The band at 1640 cm^{-1} arises more probably from a combination of Brönsted and Lewis acid sites and at 100 °C this band shows a double signal, where the band at 1635 cm^{-1} belongs to the interaction of pyridinium ion from Bronsted type sites with neutral hydrogen from adsorbed water, which disappears at 100 °C; the other band at 1615 cm^{-1} belongs to Lewis type sites; in the case of the as-synthesized materials this band is present up to about 200 °C, but in the acid type materials this band withstand temperatures up to about 400 °C. For as-synthesized MFI(ZSM5) the three bands appearing at 1443 cm^{-1}, 1490 cm^{-1} and 1596 cm^{-1} correspond exclusively to pure Lewis type sites due to the absence of Bronsted type sites (Table 3), i.e., SiO$_2$/Al$_2$O$_3$ = 120, in contrast, for MFI(ZSM5) exchanged with NH$_4$NO$_3$ and calcined the bands at 1490 cm^{-1} and 1596 cm^{-1} correspond to a combination of Lewis and Bronsted type sites, while the band appearing at 1543 cm^{-1} arises from pure Bronsted type sites. For both acidic materials, i.e. those exchanged with NH$_4$NO$_3$ and calcined at 550 °C, the two types of acid sites withstand up to about 400 °C, thus indicating a high acid strength. The amount of Brönsted and Lewis acid sites is higher in FAU(Y) zeolite (Tables 2 and 3) with respect to MFI(HZSM5), which could be due to several factors related to the zeolite structure, for example the presence of a greater amount of aluminum in the structure of FAU(Y), also the bigger size of the pore entrance in FAU(Y) should permit a better access of pyridine (kinetic diameter 0.54 nm) [53] into the channel system which,

Table 4
Crystal size and textural properties of FAU(Y).

Materials	S_{BET} (m^2/g)	V_P (cm^3/g)	D_P (nm)
Commercial zeolite[a]	619	0.38	1.8
Nanocrystaline (this work)	658	0.85	4.2

[a] Commercial: CBV720 from Zeolyst Inc.

Table 5
Crystal size and textural properties of MFI(ZSM5).

Materials	S_{BET} (m^2/g)	V_P (cm^3/g)	D_P (nm)
Commercial zeolite[a]	434	0.23	2.1
Nanocrystaline zeolite (this work)	495	0.39	2.4

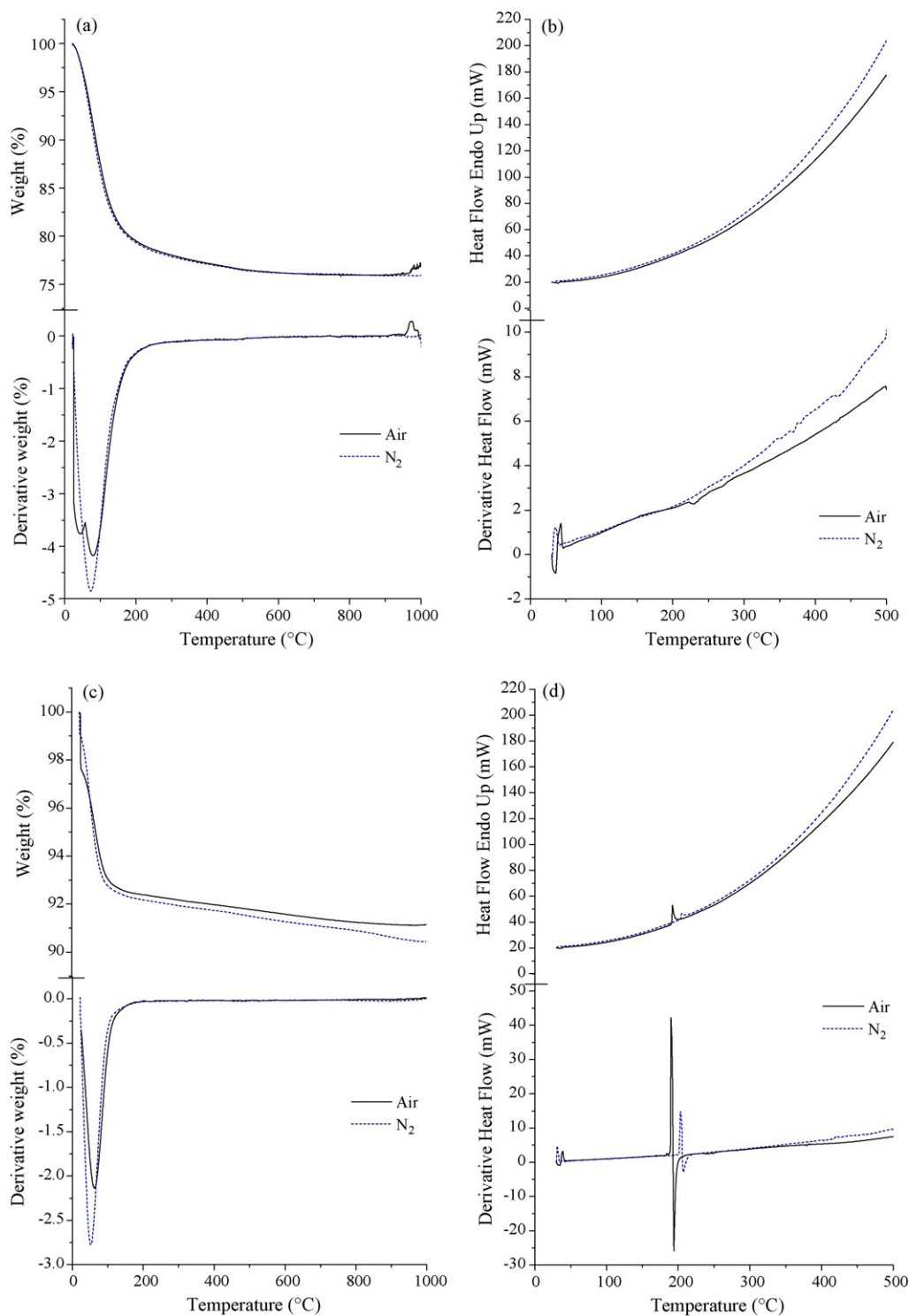[a] Commercial: CBV-1502 from Zeolyst Inc.

Fig. 12. Thermal gravimetric analysis and differential scanning calorimetry in air and N_2 atmosphere of FAU(Y) (a and b), and MFI(ZSM5) (c and d).

together with a bigger surface area (Tables 4 and 5), should allow a more wide spreaded contact between the acid sites and the pyridine molecules.

FAU(Y) and MFI(ZSM5) zeolites show an hysteresis loop of the N_2 adsorption–desorption isotherms in the range of relative pressure (P/P_0) of 0.40–1.0, strongly suggesting a mesoporosity in these materials, which agrees with results reported by Holmberg et al. [12]. Also, in both cases the nanosized zeolites presented a total surface area bigger than conventional zeolites

(Tables 4 and 5), which agrees with results reported by Larsen [20].

The weight loss in both nanocrystalline materials from room temperature to 300 °C is more probably due to a loss of moisture absorbed from the environment, and the subsequent weight loss is more probably due to organic material. The FAU(Y) lost more water with respect to MFI(ZSM5), which can be explained by the differences in the mean pore diameter and surface area of those materials. The FAU(Y) did not present any transition type during

both inert and oxidant atmosphere, but MFI(ZSM5) run in N_2 atmosphere shows a transition at 203.4 °C while under air atmosphere the transition occurs at 190.9 °C, thus suggesting the phase change of an amorphous impurity, possibly from an hydrated phase of alumina to boehmite. Afterwards the materials show a high thermal stability up to about 1000 °C.
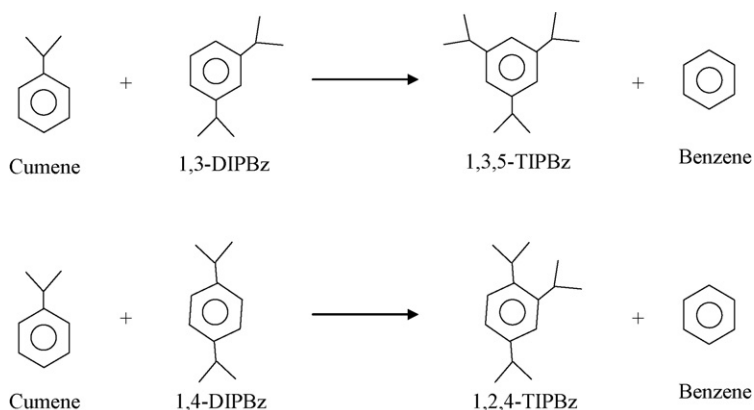
The catalytic evaluation indicates that crystals with the same or similar SiO_2/Al_2O_3 ratio but with a smaller crystal size cause the increase of cracking of 1,3,5-TIPBz, because the total external surface area increases with respect to the same mass of crystals having a bigger crystal size, thus the proportion of external surface sites increases while the diffusivity restrictions tend to diminish, as observed in Table 6.

The increase of 1,3,5-TIPBz cracking with reaction time (3–12 s) for all the materials composed by nanosized crystals is a result of a longer residence time, which implies more contacts of 1,3,5-TIPBz molecules and initial products with active sites, leading to more cracking. However, this trend is also moderated at longer residence times by the coke formation on the catalysts surface.

The cumene molecules disproportionate to form 1,3-DIPBz and 1, 4-DIPBz.

Cumene   1,3-DIPBz   Benzene

1,4-DIPBz   Benzene
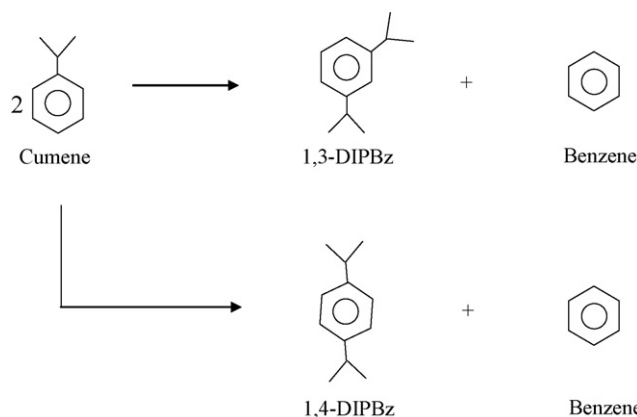
Isomers of TIPBz are formed by subsequent reactions of trans-alkylation

Cumene   1,3-DIPBz   1,3,5-TIPBz   Benzene

Cumene   1,4-DIPBz   1,2,4-TIPBz   Benzene

Regarding the various steps involved in the catalytic cracking of 1,3,5-TIPB a network of three reactions series was considered and are described schematically in the following reactions by assuming a mechanism as explained hereafter [54–56]:
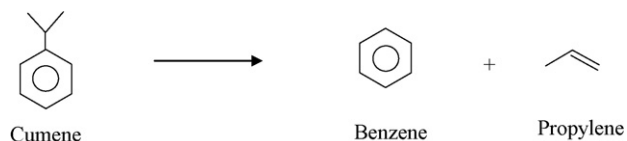
Step 1: 1,3,5-TIPBz de-alkylation occurs to produce 1,3-DIPBz and propylene.

1,3,5-TIPBz   1,3-DIPBz   Propylene
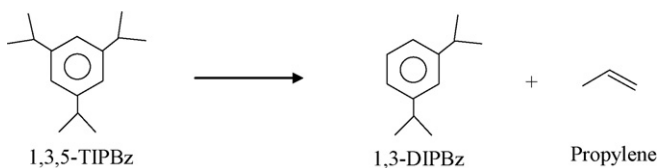
Step 2: 1,3-DIPBz de-alkylation gives cumene and propylene.

1,3-DIPBz   Cumene   Propylene
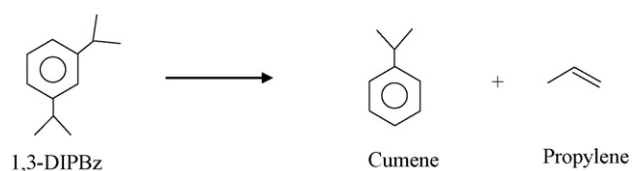
Step 3: Cumene de-alkylation forms benzene and propylene.


Cumene   Benzene   Propylene

Products of these three reactions of de-alkylation react to each other [55,56]:

For both cases, i.e., FAU(Y) and MFI(ZSM5) zeolites, the selectivity for cumene, DIPBz and Propylene ($C_3^=$), increases systematically following the crystal size diminution; the formation of benzene increases with the crystal size, which indicates that the reactions impeded by sterical conditions are favored by the diminution of the zeolites crystallite size, because a major active surface area is available, which increases the reaction speed and diminishes the diffusional restrictions of the reactive molecules (Table 6). The selectivity to cumene and DIPBz is a balance between cumene and DIPBz formation and consumption reactions. In the case of benzene, this is a product of the last step of 1,3,5-TIPBz de-alkylation and also it is a product of the reactions among products of the 1st and 2nd step of de-alkylation (i.e. disproportionation and trans-alkylation reactions), these last reactions can happen both on the acid sites present on the external surface area as well as into the inner channels, due to their kinetic diameter (i.e. cumene 0.68 nm, 1,3-DIPBz 0.84 nm and 1,4-DIPBz 0.68 nm) [55,56] which should allow these molecules to penetrate within the zeolites pore system. The smaller the crystal size the shorter the reaction pathway and this in turn should limit the formation of the benzene, on the contrary, bigger crystals should promote the formation of benzene because the longer pathway associated with the longer crystal thickness.

The increase of 1,3,5-TIPBz cracking in the nanometric FAU(Y) zeolite with respect to the nanometric MFI(ZSM5) zeolite may be due to the difference of pore dimensions of FAU(Y) zeolite, which allows bigger molecules to have access to the internal network system of FAU(Y) with respect to MFI(ZSM5). Also, FAU(Y) has a higher amount of surface acid sites due to its bigger content of framework aluminum, which agrees with the results obtained by FTIR with pyridine desorption, as shown in Tables 2 and 3.
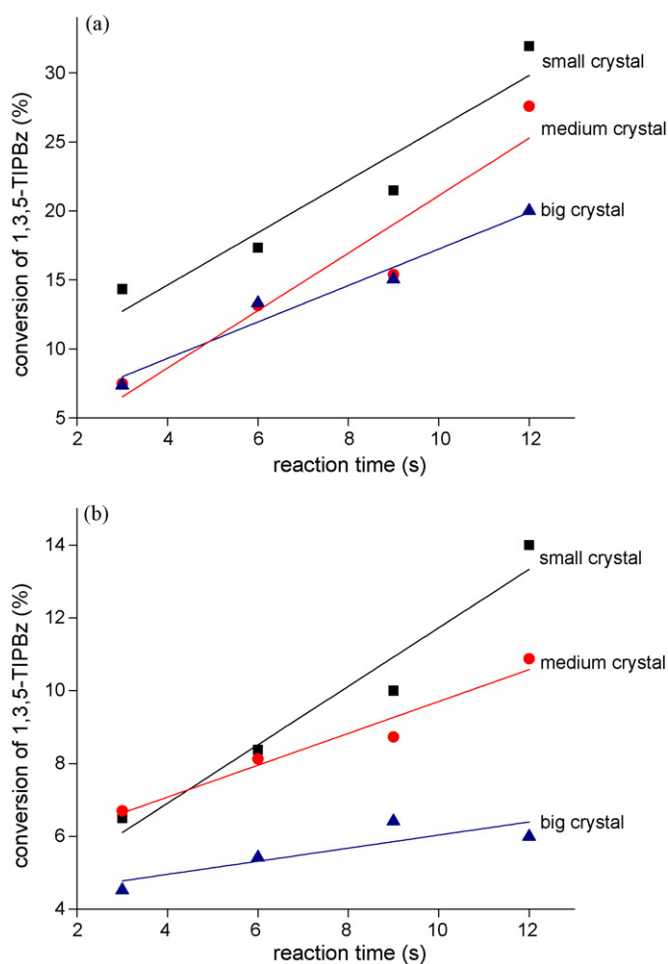
Fig. 13. Conversion of 1,3,5-TIPBz over crystalline materials with different crystal sizes and similar SiO_2/Al_2O_3 ratio: (a) FAU(Y) and (b) MFI(ZSM5). Experimental points and their average lines are shown.

Table 6
The influence of crystal size on diffusion effects in FAU(Y) and MFI(ZSM5).

Zeolite	Crystal size (nm)	K_{obs} (s^{-1})	η	φ	K_{int} (s^{-1})	D ((cm^2/s) $\times$ E-13)
FAU(Y)	18.4	0.0247	0.99	0.17	0.0249	29.23
	108.9	0.0153	0.49	1.95	0.0312	9.738
MFI(ZSM5)	20.7	0.0035	0.9918	0.17	0.0030	4.485
	82.8	0.0027	0.5868	1.56	0.0034	0.9602

5. Conclusions

The synthesized FAU(Y) and MFI(ZSM5) nanocrystals showed the typical inner structural features reported for conventional zeolites, as illustrated by the XRD Rietveld's and HRTEM methods. The mean crystal size was verified between 20 and 40 nm. The HRTEM experimental images of the inner structure of the nanometric crystallites of FAU(Y) and MFI(ZSM5) matched the simulated images, showing that the thickness of the nanocrystallites was equivalent to a few unit cells, i.e., 2–4 unit cells. Also, the presence of Bronsted and Lewis acid sites on the surface of nanometric FAU(Y) and MFI(ZSM5) seems related to the zeolite structure, structural aluminum content and pore diameters, mainly. The experimental measurements of reaction rates demonstrated that the nanosized zeolitic crystallites lead to higher conversions, in agreement with the diffusivity results (Table 6), thus the present work demonstrates the influence of the crystallite size on the catalytic activity of the FAU(Y)

and MFI(ZSM5) zeolites effects, which may be of potential interest for reaction engineering, as this is a way of improving the catalytic performance of catalysts for cracking processes and other surface dependent reactions.

References

[1] D. Barthomeuf, Basic zeolites: characterization and uses in adsorption and catalysis, Catal. Rev.: Sci. Eng. 38 (4) (1996) 521–612.
[2] J. Weitkamp, U. Weiss, S. Ernst, New aspects and trends in zeolite catalysis, Stud. Surf. Sci. Catal. 94 (1995) 363–380.
[3] C.R. Marcilly, Top. Catal. 13 (4) (2000) 357–366.
[4] A. Pfenninger, Structures and Structure Determination. Molecular Sieves: Science and Technology, vol. 2, Springer, Berlin, 1999, pp. 163–198.
[5] C.R. Marcilly, Evolution of refining and petrochemicals. What is the place of zeolites, in: Proceedings of the 13th International Zeolite Conference, Montpellier, France, July 8–13, Stud. Surf. Sci. Catal. (2001), No. 135. PL-4.
[6] (a) http://www.iza-structure.org/databases;
(b) C. Baerlocher, W.M. Meier, D.H. Olson, Atlas of Zeolite Framework Types, 5th revised ed., Elsevier, Amsterdam, 2001.
[7] O. Geier, S. Vasenkov, E. Lehmann, J. Kärger, R.A. Rakoczy, J. Weitkamp, in: Proceedings of the 13th International Zeolite Conference, Montpellier, France, July 8–13, Stud. Surf. Sci. Catal. (2001), No. 135, 19-O-04.
[8] (a) M.E. Davis, Nature 364 (1993) 291–393;
(b) T.F. Degnan Jr, J. Catal. 216 (2003) 32–46.
[9] B. Slater, C.R.A. Catlow, Molecular dynamics of the faujasite (1 1 1) surface, in: Proceedings of the 13th International Zeolite Conference, Montpellier, France, July 8–13, Stud. Surf. Sci. Catal. (2001), No. 135, 16-O-02.
[10] S. Mintova, V. Valtchev, Synthesis of nanosized FAU-type zeolite, porous materials in environmentally friendly processes, Stud. Surf. Sci. Catal. 125 (1999) 141–148.
[11] S. Mintova, V. Valtchev, T. Bein, Formation of colloidal molecular sieves: influence of silica precursor, Colloids Surf. 217 (2003) 153–157.
[12] B.A. Holmberg, H. Wang, H.M. Norbeck, Y. Yan, Controlling size and yield of zeolite Y nanocrystals using tetramethylammonium bromide, Micropor. Mesopor. Mater. 59 (2003) 13–28.
[13] B.A. Holmberg, H. Wang, Y. Yan, High silica zeolite Y nanocrystals by dealumination and direct synthesis, Micropor. Mesopor. Mater. 74 (2004) 189–198.
[14] Q. Li, D. Creaser, J. Sterte, An investigation of the nucleation/crystallization kinetics of nanosized colloidal faujasite zeolites, Chem. Mater. 14 (2002) 1319–1324.
[15] V.P. Valtchev, K.N. Bozhilov, Transmission electron microscopy study of the formation of FAU-type zeolite at room temperature, J. Phys. Chem. B 108 (2004) 15587–15598.
[16] W. Song, G. Li, V.H. Grassian, S.C. Larsen, Development of improved materials for environmental applications: nanocrystalline NaY zeolites, Environ. Sci. Technol. 39 (2005) 1214–1220.
[17] J.P. Verduijn, Exxon Chemical Patents Inc., WO 97/03020 (1997).
[18] J.P. Verduijn, Exxon Chemical Patents Inc., WO 97/03021 (1997).
[19] B.J. Schoeman, J. Sterte, Colloidal zeolite—preparation, properties and applications, Kona 15 (1997) 150–158.
[20] S.C. Larsen, Nanocrystalline zeolites and zeolite structures: synthesis, characterization, and applications, J. Phys. Chem. C 111 (2007) 18464–18474.
[21] L. Tosheva, V.P. Valtchev, Nanozeolites: synthesis, crystallization mechanism, and applications, Chem. Mater. 17 (2005) 2494–2513.
[22] S. Mintova, V. Valtchev, Effect of the source on the formation of nanosized silicalite-1: an in situ dynamic light scattering study, Micropor. Mesopor. Mater. 55 (2002) 171–179.
[23] R. Van Grieken, J.L. Sotelo, J.M. Menéndez, J.A. Melero, Anomalous crystallization mechanisms in the synthesis of nanocrystalline ZSM-5, Micropor. Mesopor. Mater. 39 (2000) 135–147.
[24] T. Tago, D. Aoki, K. Iwakai, T. Masuda, Preparation for size-controlled MOR zeolite nanocrystal using water/surfactant/organic solvent, Topics in Catalysis 52 (6–7) (2009) 865–871.
[25] J. Aguado, D.P. Serrano, J.M. Escola, J.M. Rodriguez, Low temperature synthesis and properties of ZSM5 aggregates formed by ultra-small nanocrystals, Micropor. Mesopor. Mater. 75 (2004) 41–49.
[26] W.O. Haag, R.M. Lago, P.B. Weisz, Faraday Discuss. Chem. Soc. 72 (1981) 317.
[27] P.B. Weisz, Ind. Eng. Chem. Res. 34 (1995) 2692.
[28] M. Farcasiu, T.F. Degnan, The role of external surface activity in the effectiveness of zeolites, Ind. Eng. Chem. Res. 27 (1988) 45–47.
[29] C.L. Thomas, D.S. Barmby, J. Catal. 12 (1968) 341–346.
[30] J.M. Maselli, A.W. Peters, Cat. Rev.: Sci. Eng. 26 (1984) 525.
[31] K. Rajagopalan, A.W. Peters, G.C. Edwards, Influence of zeolite particle size on selectivity during fluid catalytic cracking, Appl. Catal. 23 (1986) 69–80.
[32] M. Yamamura, K. Chaki, T. Wakatsuki, H. Okado, Synthesis of ZSM5 zeolite with small crystal size and its catalytic performance for ethylene oligomerization, Zeolites 14 (1994) 643–649.
[33] E.F.S. Aguiar, M.L. Murta-Valle, M.P. Silva, D.F. Silva, Influence of external surface area of rare-earth containing Y zeolites on the cracking of 1,3,5-triisopropylbenzene, Zeolites 15 (1995) 620–623.
[34] P. Morales-Pacheco, R.F. Alvarez, P. Del Angel, L. Bucio, J.M. Domínguez, Synthesis and structural properties of zeolytic nanocrystals I. MFI Type Zeolites, J. Phys. Chem. C 6 (2007) 2368–2378.

[35] P. Morales-Pacheco, R.F. Alvarez, L. Bucio, J.M. Domínguez, Synthesis and structural properties of zeolytic nanocrystals II. FAU type zeolites, J. Phys. Chem. C 113 (6) (2009) 2247–2255.

[36] J.M. Cowley, A.F. Moodie, Acta Crystallogr. 10 (1957) 609.

[37] HRTEM, Cerius^2 Modulus, ACCELRYS Corp., San Diego, CA, 2002.

[38] C.A. Emeis, Determination of integrated molar extinction coefficients for infrared absorption bands of pyridine adsorbed on solid acid catalysts, J. Catal. 141 (1993) 347–354.

[39] S. Batia, Zeolite Catalysis: Principles and Applications, CRC Press, Inc., Boca Raton, FL, 1989.

[40] G. De la Puente, A. Devard, U. Sedran, Conversion of residual feedstocks in FCC. Evaluation of feedstock reactivity and product distributions in the laboratory, Energy Fuels 21 (6) (2007) 3090–3094.

[41] N.Y. Chen, T.F. Degnan, C.M. Smith, Molecular Transport and Reaction in Zeolites: Design and Application of Shape Selective Catalysts, Technology & Engineering, Wiley-VCH, New York, 1994.

[42] ASTM D3906-03, Determination of relative X-ray diffraction intensities of faujasite-type zeolite-containing materials.

[43] M.M.J. Treacy, J.B. Higgins, Collection of Simulated XRD Powder Patterns for Zeolites, 5th ed., IZA, Elsevier, Amsterdam, 2007, ISBN 0444530673.

[44] D.W. Breck, Zeolite Molecular Sieves, John Wiley & Sons, Inc., 1974.

[45] D.H. Olsen, G.T. Kokotailo, S.L. Lawton, W.M. Meier, Crystal structure and structure-related properties of ZSM5, J. Phys. Chem. 89 (1981) 2238–2243.

[46] M. Niwa, T. Kunieda, J.H. Kim, ACS Symp. Ser. 738 (2000) 181.

[47] Ch. Baerlocher, W.M. Meier, D.H. Olson, Atlas of Zeolite Framework Types, 5th ed., IZA, Elsevier, Amsterdam, 2001, pp. 184–185.

[48] J.C. Jansen, F.J. Van der Gaag, H. Van Bekkum, Zeolites 4 (1984) 369.

[49] P.A. Jacobs, H.K. Beyer, J. Valyon, Zeolites 1 (1981) 161.

[50] G. Coudurier, C. Naccache, J.C. Vedrine, J. Chem. Soc., Chem. Commun. (1982) 1413.

[51] J.W. Ward, J. Catal. 9 (1967) 225.

[52] M.W. Anderson, J. Klinowski, Zeolites 6 (1986) 455.

[53] C.N. Satterfield, Mass Transfer in Heterogeneous Catalysis, MIT Press, Cambridge, MA, 1970.

[54] S. Al-Khattaf, J.A. Atias, K. Jarosch, H. de Lasa, Diffusion and catalytic cracking of 1,3,5-tri-iso-propyl-benzene in FCC catalysts, Chem. Eng. Sci. 57 (2002) 4909–4920.

[55] S. Al-Khattaf, H. de Lasa, The role of diffusion in alkyl-benzenes catalytic cracking, Appl. Catal. A: Gen. 226 (2002) 139–153.

[56] K.A. Mahgoub, S. Al-Khattaf, Catalytic cracking of hydrocarbons in a riser simulator: the effect of catalyst accessibility and acidity, Energy Fuels 19 (2005) 329–338.